

Electron and Hole Dynamics in Dye-Sensitized Solar Cells: Influencing Factors and Systematic Trends

Sheng Meng,^{*,†,‡} and Efthimios Kaxiras[‡]

[†]Beijing National Laboratory for Condensed Matter Physics and Institute of Physics, Chinese Academy of Sciences, 100190 Beijing, China, and [‡]Institute of Materials, School of Engineering, Swiss Federal Institute of Technology (EPFL), CH-1015 Lausanne, Switzerland

ABSTRACT We investigate electron and hole dynamics upon photon excitation in dye-sensitized solar cells, using a recently developed method based on real-time evolution of electronic states through time-dependent density functional theory. The systems we considered consist of organic sensitizers and nanocrystalline TiO₂ semiconductors. We examine the influence of various factors on the dynamics of electrons and holes, including point defects (vacancies) on the TiO₂ surface, variations in the dye molecular size and binding geometry, and thermal fluctuations which result in different alignments of the electronic energy levels. Two clear trends emerge: (a) dissociated adsorption of the dye molecules leads to faster electron injection dynamics by reducing interfacial dipole moments; (b) oxygen vacancy defects stabilize dye adsorption and facilitate charge injection, at the cost of lower open circuit voltage and higher electron–hole recombination rate. Understanding of these effects at the atomic level suggests tunable parameters through which the electronic characteristics of dye-sensitized solar cell devices can be improved and their efficiency can be maximized.

KEYWORDS Ultrafast dynamics, charge injection, TDDFT, solar cell, energy harvest

Among renewable energy solutions, dye-sensitized solar cells (DSSCs, also called “Grätzel cells”) have attracted much attention as an alternative inexpensive and environmentally friendly method for sunlight-to-electricity conversion.^{1–3} Such devices become even more attractive when the dye molecules are natural⁴ or organic ones^{5–8} which do not contain rare, often toxic, inorganic metal ions. The biggest challenges for developing organic-dye-based DSSCs are relatively low efficiency and limited long-term stability.⁷ Both factors depend sensitively on the structural details, binding mechanisms, and carrier dynamics at the dye–semiconductor interface. Tuning these parameters can greatly enhance the device performance, eventually leading to large-scale implementation of DSSCs for energy conversion. Experimentally, the highest efficiency achieved using this type of organic dyes⁹ is ~9%, compared to 11.2% for DSSC devices employing metal-containing dyes,³ and <6% for all-organic solar cells.⁹

A DSSC essentially comprises three important components for photocurrent generation: (i) a nanocrystalline oxide semiconductor as electrode, mostly TiO₂, responsible for photoelectron collection; (ii) dye molecules attached to the TiO₂ surface for visible light absorption; and (iii) an electrolyte, which conducts electrons from the counter-electrode to regenerate the excited dye cations.^{2,3} The semiconductor–molecule interface at which all three

components are present, where the photogenerated electrons and holes are separated, is of central importance for the performance of the device.¹⁰ Due to its complexity, a variety of factors describing this interface strongly influence the charge separation and recombination mechanism, an essential process for any type of solar cells and accounting for the overall efficiency of devices. These factors include molecular geometry, binding groups, surface orientation, defects, dissociation, pH, and additive ionic potential.^{11–14} Recently there have been a few experimental efforts attempting to resolve and rationalize how electron–hole separation and recombination processes depend on these various factors, including, for instance, anchor groups,^{13,15} bridge lengths,^{16,17} and ion concentration;¹² however, due to the complex nature of the interface system and difficulties to have correct assignments of measured signals, an explicit theoretical understanding at the single-molecule level is still lacking. This situation hinders understanding the mechanism of electron–hole separation and recombination in real devices, its dependence on various factors, and how these factors can be tuned to optimize the device performance.

In this work, we study the problems related to DSSC performance and stability at the molecular scale, using state-of-the-art first-principles calculations within the framework of time-dependent density functional theory (TDDFT).¹⁸ We illustrate in a quantitative manner how molecular size, the molecule dissociation state upon its adsorption on the semiconductor surface, and different binding configurations with or without surface defects will influence the stability and

* To whom correspondence should be addressed, smeng@iphy.ac.cn.

Received for review: 11/9/2010

Published on Web: 03/30/2010



electron dynamics at the interface between dye molecules and the TiO₂ substrate. We find that the presence of many influencing factors leads to electron injection dynamics that is dispersive in nature. By considering a wide range of possible structural and electronic configurations, we clarify how particular system features change the time scale of molecular processes such as electron injection.

In a real device, several practical aspects are also important, including contact with a transparent conducting layer, the metal electrode, the catalytic counter-electrode, and packaging issues, such as antireflection and electrolyte filling and sealing; all these play important roles in cost and environmental considerations.^{3,19} These factors are beyond the scope of what can be addressed by our work.

The calculations reported here were performed within the SIESTA code.²⁰ We use pseudopotentials of the Troullier–Martins type²¹ to model the atomic cores, the PBE form of the exchange–correlation functional,²² and a local basis set of double- ζ polarized orbitals (19 numerical atomic orbitals for Ti including semicore 3s and 3p states;²³ 13 orbitals for C, N, O, and S; 5 orbitals for H). An auxiliary real space grid equivalent to a plane-wave cutoff of 70 Ry is used for the calculation of the electrostatic (Hartree) term. Solvent molecules are not currently included in the model structures, since they participate in weaker interactions including hydrogen bonding and van der Waals forces; investigations of their influence are under way. For geometry optimization, a structure is considered fully relaxed when the magnitude of forces on the atoms is smaller than 0.04 eV/Å. Optical absorption and electron dynamics are extracted from TDDFT simulations. Optical absorbance is calculated within the linear response regime,²⁴ by propagating wave functions 6107 steps in time after abruptly turning off a perturbing external field of 0.1 V/Å. The time step of simulations is 0.0034 fs, corresponding to an energy resolution of 0.1 eV.

For the simulation of electron injection, the evolution of both electrons and ions in real time is monitored after excitation. The time-dependent Kohn–Sham equations of electrons and the Newtonian motion of ions are solved simultaneously, with ionic forces along the classical trajectory evaluated through the Ehrenfest theorem.²⁵ The electron density is updated self-consistently during the real-time propagation of single-particle Kohn–Sham wave functions with a time step of 0.02419 fs. The initial velocity of ions is assigned according to the equilibrium Boltzmann–Maxwell distribution at a given temperature (350 K) unless otherwise specified. Within this scheme, the total energy is well conserved to within 10⁻⁴ eV/fs. This convergence is by choice; better performance can be obtained if a more stringent self-consistency criterion for each time step is chosen. In practice, we have checked that this level of convergence produces negligible differences in the evolution of energy levels and electron–ion dynamics. The use of

TDDFT for treating excited states and dynamics has been debated recently^{26,27} and the latest results have shown it accurate in many applications.²⁸ Our TDDFT simulations are significantly different from quantum dynamics utilizing effective Hamiltonian²⁹ or time-domain quantum simulations,^{14,30} because we use a full TDDFT treatment of electron–ion dynamics, in which the Hamiltonian (therefore electronic coupling) is always updated and consistent with electron density at a given time, whereas other methods generally use a fixed Hamiltonian for a time span of at least 1 fs (which is 2–3 orders of magnitude larger than the time step used for wave function propagation). Since the electronic coupling between dye molecules and TiO₂ is key to electron injection processes,¹³ we believe our method produces more accurate electron couplings between the dye and TiO₂ and in turn ultrafast injection dynamics. Consequently, our calculations are quite computationally intensive: a single excited state electron–ion trajectory of 200 fs typically takes ~8300 propagation steps and only a few trajectories can be practically obtained for a given atomic configuration.

We begin by considering charge separation processes occurring at the dye–semiconductor interface. Charge separation is central for sunlight-to-electricity conversion in any type of solar cells. An efficient scheme for electron–hole dissociation comparing to other competing deactivation processes, such as recombination, implies high efficiency in photocurrent generation. However, this involves a compromise: a faster electron injection rate usually requires the energy level of the excited state in the dye molecule to be very high into the conduction band of the semiconductor, but this results in a lower open circuit voltage; this effect is referred to as the “kinetic redundancy”.^{10,12} Therefore for best device performance what is desirable is not the fastest possible charge injection but an injection rate faster than competing de-excitation channels. We construct a model that captures the essential aspects of both the semiconductor and the dye components.

Interaction between organic molecules and low-dimensional oxide semiconductors such as TiO₂ has been the subject of intensive investigations recently.^{11,29–32} For studying TiO₂ nanostructures, we construct and adopt a one-dimensional (1D) model nanowire system based on the anatase phase of TiO₂.³³ Dye solar cells employing nanowire structures^{34–37} (including nanotubes) for the photoanode have been used in experiments, usually with metal complex dyes. The advantages for this type of electrode geometry include increased photon scattering and enhanced electron transport due to its 1D geometry, as have been demonstrated experimentally.^{34–36} This 1D geometry also has certain computational advantages, since a relatively small segment can be used to adsorb a large/long dye molecule and it still captures the essential features of electronic structures of larger, bulkier particles used in experiments, as a result of the extended 1D geometry. The experimental

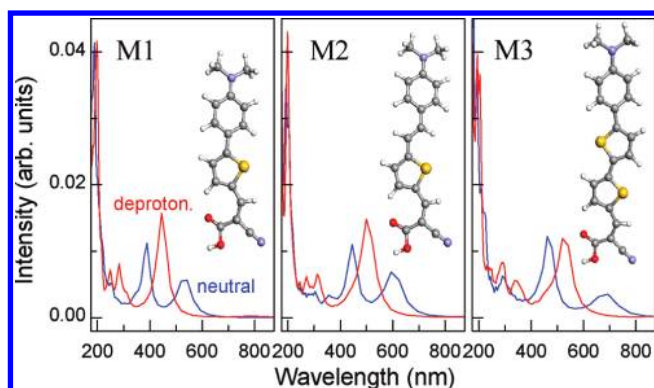


FIGURE 1. Model organic dyes considered in this work and corresponding optical absorption spectra, in the neutral form (blue line) and in the deprotonated one (red line). These dyes are modified relative to those used in experiments by substituting the end dimethylfluorene groups (M1 and M3) or phenyl groups (M2) with two methyl groups.

lattice constants³⁸ $a = b = 3.784 \text{ \AA}$ and $c = 9.515 \text{ \AA}$, which are close to the theoretical values of 3.80 and 9.53 \AA , were used for the wire structure. Periodic boundary conditions are used also in the directions perpendicular to the wire axis, which separate the nanowire from its images by at least 10 \AA of vacuum. We note that in recent experiments nanowires of similar size, as small as 5 \AA in diameter, have been synthesized and used,^{39,40} as well as nanocrystalline particles³ with a diameter of 2–8 nm. Our structures capture the realistic features of experimental counterparts (e.g., 1D geometry, orientation and facets) and serve as a reasonable model. We note that from the comparison of electronic structures, this model, despite its simplicity, captures general electronic characteristics of other low-dimensional systems, such as surfaces and nanoparticles, as discussed below.

In order to understand how the performance and in particular the electron–hole quantum dynamics are affected by the different factors at the dye–TiO₂ interface, we investigate the electron dynamics at the interface for a variety of different binding configurations among a group of model organic dyes. The molecular structure of these model dyes is shown in Figure 1. They have the same structure as those developed and used in experiment^{7,8} recently where high efficiency has been shown (8%), except that at one end of the molecule dimethylfluorene or phenyl groups are substituted by smaller hydrophobic methyl groups. These groups do not affect the optical properties of the dyes: we have analyzed the optical spectrum and corresponding wave function plots and find that the major absorption peak in the visible range comes from the transition between HOMO and LUMO states of the dye, with both orbitals located mainly on the body of the molecular chain, including the other end through which the molecule binds to semiconductor surfaces, with little weight on the end group that has been substituted. Therefore our choices represent a reasonable model for the molecular geometry, electronic structure, and dynamics for the optical transitions under

consideration. The dipole moments for the three model dyes are similar, being 11.80, 13.19, and 13.29 D (1 D = 1 debye = 0.208 e · \AA) for the M1, M2, and M3 dyes, respectively.

For further justification, Figure 1 presents optical absorption spectra for these model dyes. The calculated excitation energy for the first two absorption peaks of M1 is 2.3 and 3.2 eV, lower but comparable to the experimentally measured ones,⁷ 2.84 and 3.50 eV, respectively, due to the lack of asymptotic ($-1/r$) behavior in the PBE exchange–correlation functional to correctly describe the charge-transfer excitations.²⁶ The presence of a second thiophene group in the M3 molecule results in a red shift of the two peaks, consistent with experimental measurements,⁷ though the absolute value cannot be trusted due to the error in charge-transfer excitation energies.

Next we present some evidence for the presence of the deprotonated form of the M2 dye in ethanol solutions. The calculated spectrum for deprotonated M2 (removing the H⁺ from the cyanoacrylic acid group) has a strong absorption peak at 2.5 eV. This matches closely the experimental spectrum⁸ in ethanol where a single strong peak appears at 2.8 eV. A small peak with a higher energy is also found in both theory (3.98 eV) and experiment (4.13 eV). On the other hand, the neutral form of the M2 dye shows two prominent peaks around 2.1 and 2.8 eV, with the former being stronger, and no additional apparent peaks around 4 eV; thus it is very different from the measured spectrum.⁸ This is *not* a result of substitution of phenyl end groups with methyl groups in the model M2 molecule. As a check, we calculated the optical spectrum of the complete dye structure used in experiment (with phenyl end groups), both in neutral and in deprotonated forms, and they show exactly the same behavior as the model dye, M2, except that all peaks are 0.2 eV lower in energy due to the more severe self-interaction errors in the actual molecules used in experiment. In addition, we found that all model dyes M1, M2, M3 experience a similar behavior in optical spectrum; that is, two peaks are shifted and combined to form a single strong peak with an averaged energy after being deprotonated. In the cases of M1 and M3, the neutral form shows a spectrum that is close to experiment and therefore should be the dominant form for these molecules in solutions. The interesting difference for the dye molecular states between M1 and M3 versus M2 is attributed to the different molecular composition, that is, the presence of the C=C double bond in M2, or to different preparation processes.

Since different protonation states could be present for organic dyes, we investigated how these states, together with other geometrical changes in the molecule, affect the structural stability and dynamics at the dye–TiO₂ interface. To illustrate, we use M1 as an example and show a variety of possible molecular states and binding geometries at the interface in Figure 2. The end cyanoacrylic acid has three groups that could bind to the TiO₂ surface, via –CN–Ti, –CO–Ti, and –COH–O (–CO–Ti if H is removed) bonds;

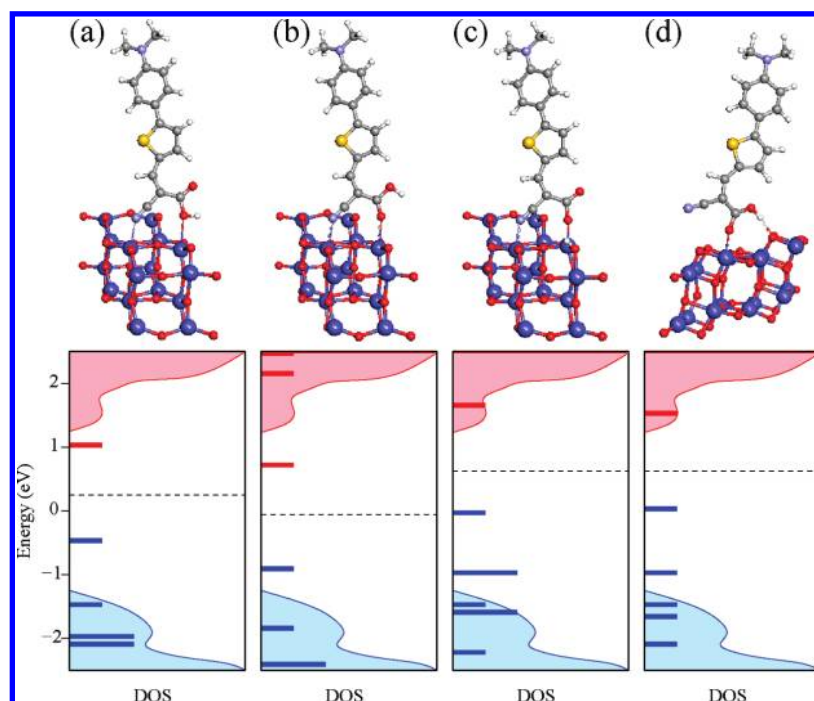


FIGURE 2. (a–d) Different binding configurations of the model dye molecule M1 bonded to the TiO_2 surface and corresponding plots of the density of states (DOS). In the latter, the shaded regions correspond to the TiO_2 -related valence (blue) and conduction (red) states. The horizontal bars represent occupied (blue) and empty (red) molecular states (singly or doubly degenerate). The dashed line is the Fermi level, defined as the midgap point between the highest occupied and lowest unoccupied electronic state, which may belong either to the molecule or to the semiconductor. The zero of the energy scale is defined as the midgap point for the semiconductor-related states only.

therefore, there are many possible binding configurations. We present a detailed characterization on several stable representative configurations and comment on other possible arrangements. Configuration (a) is a case where an intact M1 binds through both of its $-\text{CN}$ and $-\text{CO}$ groups to a 5-fold Ti ion on the TiO_2 (101) surface, which leads to a binding energy of 0.99 eV. The H atom on the $-\text{COH}$ unit can be easily transferred to the neighboring $-\text{C}=\text{O}$ group, forming configuration (b), which is more favorable than (a) by 0.066 eV per molecule. This H atom can also be removed from the molecule and placed onto the TiO_2 substrate, resulting in configuration (c) where the dye is in its dissociated form. The binding energy in configuration (c) is 0.085 eV smaller than that in (a), consistent with earlier discussion about the presence of intact versus deprotonated M1 dyes. This small energy difference is, however, at the limit of accuracy of DFT calculations. Taking into account various limitations of the model system, including the small size of the semiconductor component, the absence of solvent molecules, the surface termination and different pH values, it is likely that all configurations with similar binding energy are present in a real system. Configuration (d) is an interesting case, where the $-\text{COOH}$ group binds to the surface at steps via $-\text{C}=\text{O}-\text{Ti}$ and a hydrogen bond between $-\text{COH}$ and bridge O atoms of the TiO_2 surface. This state is the most stable among all the configurations we considered, with an energy 0.25 eV lower than configuration (a). Another important configuration, not shown in Figure 2, consists of the

dye binding to TiO_2 via a bidentate structure through the dissociated carboxylic group, as considered in ref 41. We find that this configuration has the smallest binding energy, 0.50 eV lower than that of configuration (d). Alternatively, the TiO_2 surface may be terminated by surface OH and H groups, preventing $-\text{COH}$ binding, or the dye–surface hydrogen bond, with a relatively weak strength of ~ 0.3 eV, may be displaced by solvent molecules or indirect bridging hydrogen bond networks, all of which could stabilize the dye in a realistic environment. If that happens, the resulting displaced configuration could have similar or even lower stability than other configurations. All these comparisons are based on the total energy of the combined dye/ TiO_2 system in different configurations, where all atoms have very similar positions (except for one H atom); therefore basis-set superposition errors are not important.

The diversity in stable configurations at the dye– TiO_2 interface results in a diversity in electronic structure. Specifically, due to structural differences, the relative alignment of the LUMO level of dye molecules to the conduction band of TiO_2 varies. It is typically within ± 0.3 eV of the conduction band minimum (CBM) with the exception of case (b): the dye LUMO is 0.23 eV below CBM for the intact configuration (a) and 0.32 eV above CBM for the dissociated form (c); for configuration (d), the value is 0.19 eV above CMB; all these cases could facilitate a fast electron injection from the dye LUMO to conduction band of TiO_2 . In configuration (b), however, the dye LUMO is 0.67 eV below the CBM, render-

ing efficient charge transfer unlikely even taking thermal fluctuations into account. We note that for the configuration with the bidentate carboxylic binding,⁴¹ the dye LUMO is 0.5 eV above the semiconductor CBM. However, due to its low stability (having the smallest binding energy), we did not consider this structure in more detail; we expect that this structure would lead to fast electron injection similar to cases (c) and (d). Importantly, we found that the relative band alignments discussed above do not depend on the specific TiO₂ structure we choose, namely, the 1D nanowire model. We have calculated dye adsorption on a 2D surface system (anatase (101) surface) at a similar coverage, as well as a finite (0 D) TiO₂ nanoparticle of comparable size (length, ~15 Å; width, ~6 Å). In both cases, the calculated dye LUMO levels have very close alignments to those obtained with the nanowire model. Specifically, these levels (relative to the CBM), for the four dye structures shown in Figure 2a–d, are as follows: in the nanowire (−0.23, −0.69, +0.32, +0.19 eV), in the surface (−0.28, −0.73, +0.26, +0.17 eV), in the nanoparticle (−0.24, −0.55, +0.52, +0.19 eV).

The alignment between dye molecular orbitals and the TiO₂ bands in different configurations has its origin in the dipole moment at the interface. A dipole pointing outward from the TiO₂ surface (negative pole) to the dye molecule (positive pole) will give rise to a surface potential which pulls down the dye orbitals relative to CBM. The interface dipole moments along the long axis of the dye molecules are 18.56, 22.75, and 11.62 D for molecular configurations (a), (b), and (d) in the ground state, and 23.16, 26.90, and 19.90 D in the excited state, pointing outward from the surface. The magnitude of the interface dipole moment is consistent with the position of the H atom involved in dissociation in these three geometries. The larger the interfacial dipole moment, the lower the dye LUMO relative to the CBM of TiO₂, as is observed in Figure 2. This point is also consistent with a previous study of the band alignments at the interface between metal complexes and TiO₂ in the ground state.³² In order to explain the observed large open circuit voltage in a solid-state DSSC,⁴¹ it has been argued that a positive dipole at the interface results in an upshift of CBM. This is consistent with our results.

It would be interesting to know how these diverse structural arrangements of the dye–TiO₂ interface affect electron and hole dynamics, an issue of central importance for sunlight harvest and conversion. We studied this problem by molecular dynamics simulation of the excited-state electron–ion evolution. Typically for a given system of dye/TiO₂, we first promote one electron from the dye HOMO to the dye LUMO level at time $t = 0$ for the first excited state. Then we evolve all the occupied electronic states based on TDDFT and propagate ionic positions according to classical Newtonian dynamics. The two are coupled in a coherent way, with the electronic degrees of freedom evolving in the potential created by the moving ions and the ions moving according to the forces which are a functional of the time-

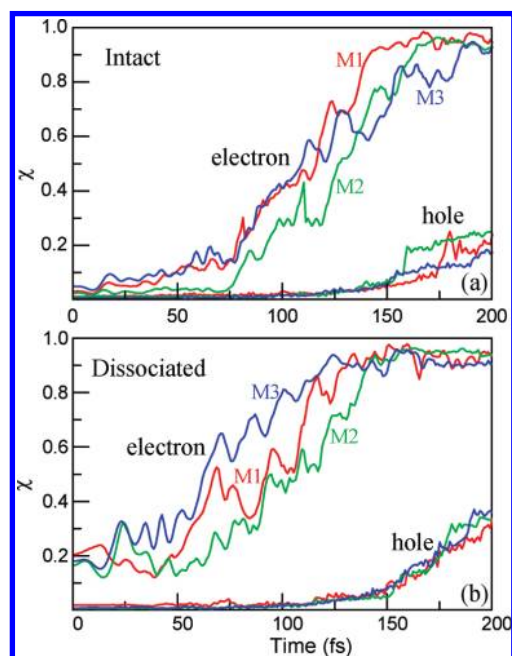


FIGURE 3. Comparison of electron (solid lines) and hole (dashed lines) dynamics of the M1, M2, and M3 model dyes, in intact and dissociated forms. χ is defined in eq 1 and represents the injection probability.

dependent electronic density (Ehrenfest dynamics). In order to determine the amount of charge transfer, we use the integral of excited electron (hole) density projected onto the TiO₂ orbitals, χ , as a function of time after photon absorption, with χ defined as

$$\chi = \int d\mathbf{r} |\tilde{\psi}(\mathbf{r})|^2, \quad \tilde{\psi}(\mathbf{r}) = \sum_{j \in \text{TiO}_2} c_j \phi_j(\mathbf{r}) \quad (1)$$

where c_j are the coefficients of atomic basis states ϕ_j in the Kohn–Sham orbital $\psi_{\text{KS}}(\mathbf{r})$ of interest (either the excited electron or the hole)

$$\psi_{\text{KS}}(\mathbf{r}) = \sum_j c_j \phi_j(\mathbf{r}) \quad (2)$$

The electron and hole dynamics for M1, M2, and M3 dyes are shown in Figure 3. It is clear that after excitation, the electron gradually delocalizes and is injected into the semiconductor region, on a time scale of 125–175 fs (Table 1), while at this time the corresponding hole stays in the dye molecule and does not penetrate through the interface region. The hole injection time is much longer than the time for electron injection, and hole injection only starts after the excited electron has been completely injected into the TiO₂ and, therefore, could be influenced by the injected electrons due to the small size of our TiO₂ model. The injected electron

TABLE 1. Comparison of Experimental and Calculated Electron Injection Times from Various Dye Molecules to TiO₂ Conduction Bands^a

| | sensitizer | time (fs) | references | |
|---------------------|--|---------------|----------------|--------------|
| metal complexes | Ru(4,4'-COOH-2,2'-bipyridine) ₂ (NCS) ₂ (N3) | <150, ~50 | refs 42 and 43 | |
| | Zn phthalocyanine with tyrosine (ZnPcTyr) | 160 | ref 44 | |
| | Re(CO) ₃ Cl (dcbpy) | <100 | ref 16 | |
| | Zn porphyrin derivatives | <250 | ref 45 | |
| | Zn porphyrins with phenylethynyl linkers | 200–300 | ref 17 | |
| metal-free organics | anthocyanin | <100 | ref 46 | |
| | alizarin | 6 | ref 47 | |
| | bi-isonicotinic acid | 3 | ref 48 | |
| | perylene (DTB-Pe) | 75 | ref 49 | |
| | perylene (DTB-Pe-rod, DTB-Pe-tripod) | 240, 970 | ref 15 | |
| | fluorescein 27 | 300 | ref 50 | |
| | coumarin 343 | 180, 125 ± 25 | refs 51 and 52 | |
| | aminophenyl acids (NK1, NK2, NK7) | <40, 240–270 | ref 53 | |
| | theory | M1 | 141 | present work |
| | | M2 | 162 | present work |
| M3 | | 184 | present work | |

^a Only fastest components are included for multiexponential injection kinetics. Theoretical results are based on nondissociated cases in Figure 3a; see text for details.

dissipates into the d_{xy} orbitals of Ti ions, which constitute the lowest conduction bands of the semiconductor. Therefore, the electron–hole pair generated by photon absorption will split in space, within a time scale of ~200 fs.

The above process is a result of energy level alignments at the dye–TiO₂ interface. In a DSSC the lowest unoccupied molecular orbital (LUMO) of the dye molecule should be higher in energy than the CBM and close to it. These states are very close in energy and strongly coupled and can be easily mixed due to thermal fluctuations. On the other hand, since the dye molecules have a smaller energy gap (~2 eV) than the oxide semiconductor TiO₂ (3.4 eV), the dye's highest occupied molecular orbital (HOMO) is in the band gap region, with a large energy separation (>1.5 eV) to the valence band of TiO₂. The mixing of the HOMO and the valence band is much slower, resulting in stable hole dynamics being confined in the dye molecule.

We next focus on the effects of dye molecular dissociation onto the electron injection dynamics. Figure 3 shows excited electron dynamics for the intact and dissociated forms of model dyes M1, M2, and M3 upon photon excitation. For M1 in the intact configuration Figure 2a, the electron injection has finished at around 140 fs. Electron injection in the dissociated configuration Figure 2c is faster than in the intact configuration Figure 2a, typically by 10–15 fs. The same trend is true for the M2 and M3 dyes: dye dissociation makes the electron injection faster. For instance, the charge injection for the dissociated M3 molecule, in a geometry similar to Figure 2c, is 60–70 fs faster than that in the intact configuration, consistent with earlier discussion. This can be explained by the fact that after dye dissociation, the H atom is moved from the molecule to the TiO₂ substrate, which has the effect of significantly reducing the interface dipole moment and affecting local reorganization, thus lowering the barrier for electron injection. Generally, dissociated dyes have LUMO levels >0.1 eV higher than intact ones. This is consistent with experimental observations that by tuning the

concentration of additive ions (such as Li⁺), a shift in the band edge by 0.1 eV results in 2-fold retardation in electron injection.¹² The retardation effect in our simulations is less pronounced because in the relatively small TiO₂ structural models we used, the energy level oscillations are large due to significant thermal fluctuations and because DFT does not accurately predict the absolute band alignments at interfaces.

We also compare how the molecular size influences the injection dynamics at the dye–TiO₂ interface. In Figure 3, we compare model dye M1 with M2 and M3, in both the intact and dissociated forms as those in parts a and c of Figure 2. In the initial stage starting from $t = 0$ to 120 fs, electron injection curves are very close to each other, but beyond this time interval, M3 has a much slower charge injection than M1, with an overall injection time of ~200 fs for M3. The initial similar injection dynamics is due to the fact that the two molecules bind to the TiO₂ surface in the same manner, and the longer overall time scale in M3 is attributed to its chain length, which is longer by a thiophene unit than the dye M1, as might be expected from intuition. The quantitative characterization presented here is a useful confirmation that intuitive arguments can serve as a guide for dye selection and optimization in combination with other factors such as extinction coefficient and molecular binding. For nonadiabatic electron transfer, an exponential decay of transfer time with respect to bridge length is expected because of the exponential decay of coupling strength with distance in a tunneling process.¹⁷ Practically, the injection time is extended by a factor of 3.3 with the addition of one CH₂ group.¹⁶ Experimental measurements indeed show that adding two CH₂ bridge groups to the Redye ReC1A, the injection time is extended by a factor of 13.7.¹⁶ By adding a (CH)₂ and a thiophene group to M1, we observe that injection times are extended by factors of 1.15 and 1.30 only. This result can be understood in two ways:

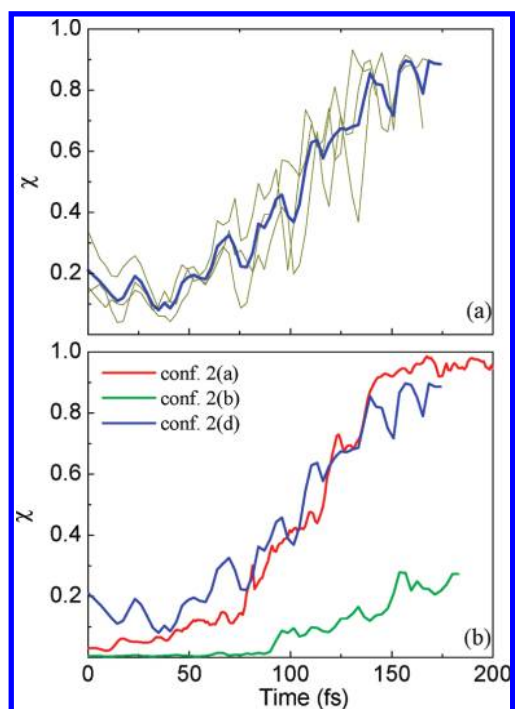


FIGURE 4. (a) Thin lines: electron injection dynamics for configuration 2(d), excited at different times separated by 200 fs in a ground-state MD trajectory; thick (blue) line: injected electrons averaged over the three cases. χ is defined in eq 1 and represents the probability of electron injection. (b) Comparison of electron injection dynamics for the three molecular configurations considered in this work: configuration 2(a), red line; configuration 2(b), green line; and averaged result for configuration 2(d), blue line.

(i) Since all M1–M3 dyes form strong covalent bonds with TiO₂, electron injection could exhibit strong adiabatic character, which does not follow exponential decay.

(ii) This is more reasonable when taking into account that from the strong light absorber, the first thiophene group, to TiO₂, the three dyes M1, M2, and M3 share the same molecular bridge for electron injection, and that addition of (CH)₂ and thiophene groups is above this absorber center; therefore the effective elongation of the electron transfer *bridge* is much reduced. Indeed, experiments on porphyrins with oligo(phenylethynyl) bridges showed similar injection times around 200–300 fs for dyes with one and four bridge groups.¹⁷ Indirect injection through shortcuts might be another important reason.

In order to see how thermal fluctuations affect the charge injection, in Figure 4a we plot electron dynamics for a set of different starting geometries for the most stable configuration in vacuum, that is, the configuration of Figure 2d. These starting geometries and ion velocities are obtained from a ground state *ab initio* molecular dynamics trajectory at 350 K and are separated in time by 200 fs from one another. The electron dynamics averaged over these trajectories is also presented in this figure. Although large fluctuations are observed for each excited state trajectory, overall they overlap very well and yield an average injection time of ~140 fs. This time scale is almost exactly the same as

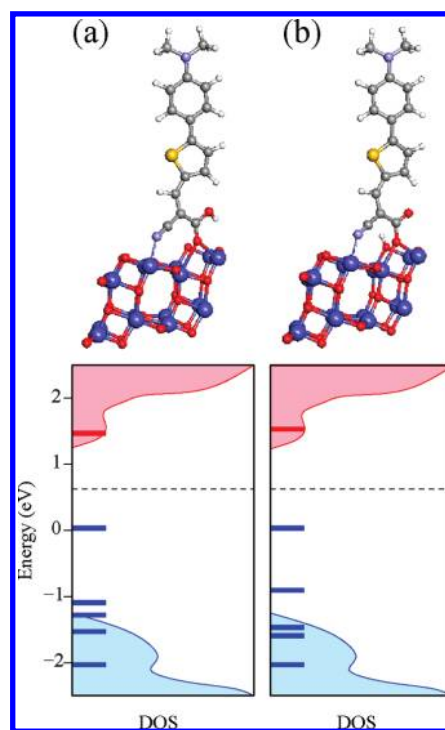


FIGURE 5. Two different configurations of the molecule M1 bonded to the O vacancy site of TiO₂ in (a) intact and (b) dissociated forms. Notation is the same as that given in Figure 2.

the configuration (a), another intact adsorption state; the comparison is shown in Figure 4b. We also found cases (not presented here) where charge injection proceeds much slower or even is reversed in a short time (within 200 fs). This leads us to conclude that although attaching via different binding groups (O(N)–Ti vs O–Ti and hydrogen bonding), the molecular binding configurations give very close injection times for the model systems studied. Charge injection in configuration 2(d) is quite different from other cases (dissociated state, or cases with defects, Figure 5, discussed below). In particular, it is different from another case for molecular adsorption, configuration 2(b), where H is transferred to the upper O atom in the binding –COOH group. The higher H position in the dye leads to an increase of the interface dipole moment and a slower electron injection time >200 fs.

For a direct comparison to experiment, we summarize in Table 1 available measurements on electron injection from various dye molecules to TiO₂. Experimentally this ultrafast injection process can be probed by time-resolved transient absorption of dye cations or injected electrons, which is the most popular, or fluorescence spectroscopy and surface science measurements such as two-photon photoemission.¹¹ In the latter case, ideal conditions such as high vacuum and single crystals are usually required and the results can be directly compared with transient measurements on nanoparticles to reveal the nature of electron injection under ideal and real conditions.¹⁵ Table 1 shows that for both metal-containing complexes and metal-free

organic dyes, the fastest component of electron injection is generally completed within 300 fs. Metal complexes usually demonstrate multiexponential injection kinetics, generally assigned to injection from unthermalized singlet excited states (~ 100 fs) and from triplets after internal relaxation (1 ps and slower); for reasons of relevance to the present work, only the former types of measurements are included in Table 1. Some processes occur at a sub-10-fs time scales for small organic dyes due to strong electronic coupling between the dye and TiO_2 and the small size of the sensitizer.^{47,48} Variations in the measured time scales for the same type of dyes come either from instrumental limitations in measuring ultrafast processes or from the fact that a variety of dye binding geometries and surface defects are present. In actual devices, the presence of ion additives, different pH, and solvents can largely tune the surface potential of the semiconductor; consequently injection times slowed down by orders of magnitude, reaching hundreds of picoseconds, have been reported^{10,12} and these numbers are not listed in Table 1.

A recent study on aminophenyl acid dye sensitizers (NK1, NK7) reports injection times of about 40 fs and < 300 fs to TiO_2 colloid particles.⁵³ These dyes have a very similar molecular structure to the model dyes presented here: NK1 differs from M1 by removing the thiophene unit and adding a $(\text{CH}_2)_2$ group and from M2 by only a thiophene unit. NK7 is closer to the original dyes to which M1–M3 resemble, in that the end CH_3 groups are replaced by phenyl groups. From the similarity in molecular structure one would expect that electron injection dynamics is similar for the two groups of dyes. Indeed, our TDDFT quantum dynamic simulations indicate that the injection time for M1–M3 ranges from 140 to 180 fs, consistent with experiment. To quantify the results of the simulations, we define the calculated injection time as the time at which the electron density injected on TiO_2 first reaches 90% and stays at this level or higher for the rest of the simulation. On the basis of this criterion, the injection time for intact M1, M2, and M3 on TiO_2 is 141, 162, and 184 fs, respectively, as listed in Table 1. For comparison, shorter time scales of 130, 140, and 150 fs are obtained for dissociated M1–M3 dyes, respectively. Our results explicitly suggest that in addition to the fast sub-40-fs component, the time scale at 250 fs in experiment⁵³ should be assigned as a major injection channel for NK1–NK7 dyes. Overall our calculated times agree well with experimental values; quantitative difference could come from uncertainties in dye aggregation, molecular structure difference, and nanoparticle geometries, etc. For instance, binding geometries similar to configuration (b) result in an injection time 2–3 folds longer, closer to experimental values.⁵³ The use of 1D nanowires instead of nanoparticles in our model may also facilitate electron injection. In general, our results present similar time scales as those measured for dyes of similar size, shown in Table 1.

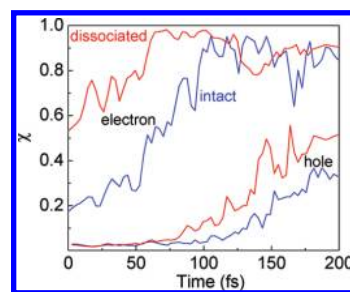


FIGURE 6. Electron (solid line) and hole (dashed line) injection from the intact (blue) and dissociated (red) form of the M1 dye to TiO_2 upon adsorption onto the O-vacancy site.

In reality, bridging O atoms at the TiO_2 surface could be missing, forming surface O vacancies. Experimentally surface O vacancies are found to be present on the anatase TiO_2 (101) surface in STM measurements.⁵⁴ The organic dye can bind around the O vacancy by inserting the O atom from $-\text{COOH}$ into the position of the vacancy. The binding of the dye molecule could take either the intact form (Figure 5a) or the dissociated one (Figure 5b). In either case we find a much greater binding energy than on a defect-free surface, 2.56 and 2.68 eV for intact and dissociated adsorption, respectively. Subsurface O vacancies, which are dominant in low-temperature STM experiments,⁵⁴ will be the subject of future studies. With the dye adsorption, the localized defect state introduced by the O vacancy is moved to higher energy, 0.1–0.2 eV below the CBM. Since the PBE functional was shown⁵⁵ inadequate to describe the localized nature of the defect state in TiO_2 , we refrain from further analysis of this issue, though in our case the problem is less severe since the O vacancy is partially filled up by the O atom from the dye. For dye adsorption around the O vacancy (charged 2+ to remove the defect state occupation), the dye LUMO is located inside the conduction band, being 0.4–1.0 eV higher than the conduction band minimum.

The injection dynamics around the O-vacancy defect has the fastest time scale, as shown in Figure 6. Electrons typically inject into the conduction band within 100 fs in the intact form, 30–40 fs faster than on the defect-free TiO_2 surface. Moreover, in dissociated M1 adsorption, charge injection is completed within 59 fs, starting from an initial hybrid state where a significant fraction (0.5 e) of the excited electron already has been transferred into TiO_2 orbitals. Therefore, in principle the charge injection can be tuned by changing the parameters during the DSSC fabrication, favoring intact or dissociated form (by changing the pH), or introducing a higher concentration of surface defects if faster electron injection is needed. Interestingly the time scale for electron injection from the dissociated M1 dye to defected TiO_2 surface, about 50 fs, is very close to the fastest injection time of ~ 40 fs in emission decay measurement for NK1 dyes.⁵³ This leads us to suggest that the fast injection time at 40 fs observed in experiment might be a result of defect states. This is an interesting possibility and a specific example of the insights that our simulations can provide.

It is important to note that although the presence of O-vacancy defects seems to enhance electron injection, the probability of charge recombination is also increased. As indicated in Figure 6, a dip in the amount of electron transfer at ~ 170 fs (130 fs) and peaks in hole transfer are observed for the intact (dissociated) dye adsorption, after the electron has been fully injected into TiO_2 . The reason is that the injected electron can be easily trapped by the local defect state, which is low in energy and very close to the half-filled HOMO state, providing an efficient recombination pathway between the CBM and the dye HOMO via the defect states. Further details are obtained by the Landau–Zener transition⁵⁶ probability between the occupied conduction band and the empty dye molecular orbitals (see Supporting Information). This probability increases from zero to $>80\%$ at the times of ~ 66 and ~ 100 fs. The state mixing is clearly monitored from the evolution of the energy levels of the dye– TiO_2 interface, where the occupied conduction band approaches the empty dye LUMO state and the two energies coincide in the time interval at 60–100 fs. Therefore, the surface O vacancies could serve as recombination centers when fast electron dynamics is not required.

In conclusion, we have investigated electron dynamics at a model dye–semiconductor interface and found that it is influenced by a number of different parameters, including dye species, molecular size, binding groups, and surface defects. Different adsorption configurations of the intact dye exhibit a similar electron injection time scale ~ 150 fs, which is 30–50 fs slower than dissociative adsorption. The efficiency of charge injection at an O-vacancy defect is significantly improved at the cost of faster recombination, while dyes with longer molecular chains show a systemically slower injection rate. Significant variability is present at the dye– TiO_2 interface, in both geometric arrangements and electronic structure. As a result, electron injection dynamics is strongly influenced by various factors; more importantly, the time scale for injection can be tuned by changing these parameters. For all the cases we studied, electron injection is very fast, it is completed in less than 200 fs, and is significantly faster than competing de-excitation channels such as back transfer and recombination, which occur on time scales an order of magnitude longer.

Acknowledgment. We acknowledge helpful suggestions and discussions with Professor M. Grätzel. S. M. is supported by the Hundred-Talent program of CAS.

Supporting Information Available. A figure showing Landau–Zener probability of an injected electron mixing with the dye LUMO state on a nanocrystalline TiO_2 with an O vacancy and energy level evolution of corresponding electronic states. This material is available free of charge via the Internet at <http://pubs.acs.org>.

REFERENCES AND NOTES

- O'Regan, B.; Grätzel, M. *Nature* **1991**, *353*, 737–740.
- Grätzel, M. *J. Photochem. Photobiol., C* **2003**, *4*, 145–153.
- Grätzel, M. *Chem. Lett.* **2005**, *34*, 8–13.
- Chapbell, W. M.; Jolley, K. W.; Wagner, P.; Wagner, K.; Walsh, P. J.; Gordon, K. C.; Schmidt-Mende, L.; Nazeeruddin, M. K.; Wang, Q.; Grätzel, M.; Officer, D. L. *J. Phys. Chem. C* **2007**, *111*, 11760–11762.
- Horiuchi, T.; Miura, H.; Uchida, S. *Chem. Commun.* **2003**, 3036.
- Ito, S.; Zakeeruddin, S. M.; Humphry-Baker, R.; Liska, P.; Charvet, R.; Pascal, C.; Nazeeruddin, M. K.; Pechy, P.; Takata, M.; Miura, H.; Uchida, S.; Grätzel, M. *Adv. Mater.* **2006**, *18*, 1202–1205.
- Kim, S.; Lee, J. K.; Kang, S. O.; Ko, J.; Yum, J. H.; Fantacci, S.; De Angelis, F.; Di Censo, D.; Nazeeruddin, M. K.; Grätzel, M. *J. Am. Chem. Soc.* **2006**, *128*, 16701–16707.
- Hagberg, D. P.; Yum, J. H.; Lee, H. J.; De Angelis, F.; Marinado, T.; Karlsson, K. M.; Humphry-Baker, R.; Sun, Hagfeldt, A.; Grätzel, M.; Nazeeruddin, M. K. *J. Am. Chem. Soc.* **2008**, *130*, 6259–6266.
- Peet, J.; Kim, J. Y.; Coates, N. E.; Ma, W. L.; Moses, D.; Heeger, A. J.; Bazan, G. C. *Nat. Mater.* **2007**, *6*, 497–500.
- Haque, S. A.; Palomares, E.; Cho, B. M.; Green, A. N. M.; Hirata, N.; Klug, D. R.; Durrant, J. R. *J. Am. Chem. Soc.* **2005**, *127*, 3456–3462.
- Anderson, N. A.; Lian, T. *Annu. Rev. Phys. Chem.* **2005**, *56*, 491–519.
- Koops, S. E.; O'Regan, B. C.; Barnes, P. R. F.; Durrant, J. R. *J. Am. Chem. Soc.* **2009**, *131*, 4808–4818.
- Ernstorfer, R.; Gundlach, L.; Felber, S.; Storck, W.; Eichberger, R.; Willig, F. *J. Phys. Chem. B* **2006**, *110*, 25383–25391.
- Duncan, W. R.; Craig, C. F.; Prezhdo, O. V. *J. Am. Chem. Soc.* **2007**, *129*, 8528–8543.
- Gundlach, L.; Ernstorfer, R.; Willig, F. *J. Phys. Chem. C* **2007**, *111*, 13586–13594.
- Asbury, J. B.; Hao, E.; Wang, Y.; Lian, T. *J. Phys. Chem. B* **2000**, *104*, 11957–11964.
- Chang, C. W.; Luo, L.; Chou, C. K.; Lo, C. F.; Lin, C. Y.; Hung, C. S.; Lee, Y. P.; Diau, E. W. *J. Phys. Chem. C* **2009**, *113*, 11524–11531.
- Runge, E.; Gross, E. K. U. *Phys. Rev. Lett.* **1984**, *52*, 997.
- Yum, J. H.; Chen, P.; Grätzel, M.; Nazeeruddin, M. K. *ChemSusChem* **2008**, *1*, 699–707.
- Soler, J. M.; Artacho, E.; Gale, J. D.; Garcia, A.; Junquera, J.; Ordejon, P.; Sanchez-Portal, D. *J. Phys.: Condens. Matter* **2002**, *14*, 2745–2779.
- Troullier, N.; Martins, J. L. *Phys. Rev. B* **1991**, *43*, 1993–2006.
- Perdew, J. P.; Burke, K.; Ernzerhof, M. *Phys. Rev. Lett.* **1996**, *77*, 3865–3868.
- Junquera, J.; Zimmer, M.; Ordejon, P.; Ghosez, Ph. *Phys. Rev. B* **2003**, *67*, 155327.
- Tsolakidis, A.; Kaxiras, E. *J. Phys. Chem. A* **2005**, *109*, 2373–2380.
- Meng, S.; Kaxiras, E. *J. Chem. Phys.* **2008**, *129*, No. 054110.
- Dreuw, A.; Head-Gordon, M. *J. Am. Chem. Soc.* **2004**, *126*, 4007–4016.
- Levine, B. G.; Ko, C.; Quenneville, J.; Martinez, T. J. *Mol. Phys.* **2006**, *104*, 1039–1051.
- Burke, K.; Werschnik, J.; Gross, E. K. U. *J. Chem. Phys.* **2005**, *123*, No. 062206.
- Rego, L. G. C.; Batista, V. S. *J. Am. Chem. Soc.* **2003**, *125*, 7989–7997.
- Duncan, W. R.; Prezhdo, O. V. *Annu. Rev. Phys. Chem.* **2007**, *58*, 143–184.
- Persson, P.; Lundqvist, M. J.; Ernstorfer, R.; Goddard III, W. A.; Willig, F. *J. Chem. Theory Comput.* **2006**, *2*, 441–451.
- De Angelis, F.; Fantacci, S.; Selloni, A.; Grätzel, M.; Nazeeruddin, M. K. *Nano Lett.* **2007**, *7*, 3189–3195.
- Meng, S.; Ren, J.; Kaxiras, E. *Nano Lett.* **2008**, *8*, 3266–3272.
- Law, M.; Greene, L. E.; Johnson, J. C.; Saykally, R.; Yang, P. *Nat. Mater.* **2005**, *4*, 455–459.
- Tan, B.; Wu, Y. Y. *J. Phys. Chem. B* **2006**, *110*, 15932–15938.
- Zhu, K.; Neale, N. R.; Miedaner, A.; Frank, A. J. *Nano Lett.* **2007**, *7*, 69–74.
- Feng, X.; Shankar, K.; Varghese, O. K.; Paulose, M.; Latempa, T. J.; Grimes, C. A. *Nano Lett.* **2008**, *8*, 3781–3786.

- (38) Mor, G. K.; Varghese, O. K.; Paulose, M.; Shankar, K.; Grimes, C. A. *Sol. Energy Mater. Sol. Cells* **2006**, *90*, 2011–2075.
- (39) Liu, C.; Yang, S. *ACS Nano* **2009**, *3*, 1025–1031.
- (40) Berger, T.; Lana-Villarreal, T.; Monllor-Satoca, D.; Gomez, R. *Chem. Phys. Lett.* **2007**, *447*, 91–95.
- (41) Chen, P.; Yum, J. H.; De Angelis, F.; Mosconi, E.; Fantacci, S.; Moon, S.-J.; Baker, R. H.; Ko, J.; Nazeeruddin, M. K.; Grätzel, M. *Nano Lett.* **2009**, *9*, 2487–2492.
- (42) Tachibana, Y.; Moser, J. E.; Grätzel, M.; Klug, D. R.; Durrant, J. R. *J. Phys. Chem.* **1996**, *100*, 20056–20062.
- (43) Ellingson, R. J.; Asbury, J. B.; Ferrere, S.; Ghosh, H. N.; Sprague, J. R.; Lian, T.; Nozik, A. J. *J. Phys. Chem. B* **1998**, *102*, 6455–6458.
- (44) He, J.; Benko, G.; Korodi, F.; Polivka, T.; Lomoth, R.; Akermark, B.; Sun, L.; Hagfeldt, A.; Sundström, V. *J. Am. Chem. Soc.* **2002**, *124*, 4922–4932.
- (45) Mozer, A. J.; Griffith, M. J.; Tsekouras, G.; Wagner, P.; Wallace, G. G.; Mori, S.; Sunahara, K.; Miyashita, M.; Earles, J. C.; Gordon, K. C.; Du, L.; Katoh, R.; Furube, A.; Officer, D. L. *J. Am. Chem. Soc.* **2009**, *131*, 15621–15623.
- (46) Cherepy, N. J.; Smestad, G. P.; Gratzel, M.; Zhang, J. Z. *J. Phys. Chem. B* **1997**, *101*, 9342–9351.
- (47) Huber, R.; Moser, J. E.; Grätzel, M.; Wachtveitl, J. *J. Phys. Chem. B* **2002**, *106*, 6494–6499.
- (48) Schnadt, J.; Bruhwiler, P. A.; Patthey, L.; O’Shea, J. N.; Sodergren, S.; Odelius, M.; Ahuja, R.; Karis, O.; Bassler, M.; Persson, P.; Siegbahn, H.; Lunell, S.; Martensson, N. *Nature* **2002**, *418*, 620–623.
- (49) Zimmermann, C.; Willig, F.; Ramakrishna, S.; Burfeindt, B.; Pettinger, B.; Eichberger, R.; Storck, W. *J. Phys. Chem. B* **2001**, *105*, 9245–9253.
- (50) Hilgendorff, M.; Sundstrom, V. *J. Phys. Chem. B* **1998**, *102*, 10505–10514.
- (51) Rehm, J. M.; McLendon, G. L.; Nagasawa, Y.; Yoshihara, K.; Moser, J.; Grätzel, M. *J. Phys. Chem.* **1996**, *100*, 9577–9578.
- (52) Ghosh, H. N.; Asbury, J. B.; Lian, T. *J. Phys. Chem. B* **1998**, *102*, 6482–6486.
- (53) Myllyperkio, P.; Manzoni, C.; Polli, D.; Cerullo, G.; Korppi-Tommola, J. *J. Phys. Chem. C* **2009**, *113*, 13985–13992.
- (54) He, Y.; Dulub, O.; Cheng, H.; Selloni, A.; Diebold, U. *Phys. Rev. Lett.* **2009**, *102*, 106105.
- (55) Di Valentin, C.; Pacchioni, G.; Selloni, A. *Phys. Rev. Lett.* **2006**, *97*, 166803.
- (56) Desouter-Lecomte, M.; Lorquet, J. C. *J. Chem. Phys.* **1979**, *71*, 4391–4403.